Wavepacket dynamics and quantum scattering in spin-orbit induced excitation and quenching in $N^+(^3P)$–$He(^1S)$ and $N^+(^1D)$–$He(^1S)$ collisions

T. Jíra
Department of Physical Chemistry, University of Chemistry and Technology, Prague 6 16628, Czech Republic

Å. Larson
Department of Physics, Stockholm University, AlbaNova University Center, S-106 91 Stockholm, Sweden

L. Aissaoui
Department of Physics, Laboratoire de Physique des Rayonnements et leurs Interactions avec la Matière, University of Batna 1 Hadj Lakhdar, Batna 05000, Algeria

M. Buchowiecki*
Institute of Physics, University of Szczecin, Wielkopolska 15, 70-451 Szczecin, Poland

(Received 2 April 2026; accepted 18 August 2026; published 3 September 2026)

The nonadiabatic wavepacket dynamics is used to calculate the excitation and quenching cross sections in the $N^+(^3P)$–$He(^1S)$ and $N^+(^1D)$–$He(^1S)$ collisions using potential energy curves and spin-orbit coupling elements calculated *ab initio*. The results are verified by comparison with cross sections calculated by solving the time-independent coupled Schrödinger equation with the logarithmic derivative method, as well as with cross sections calculated semiclassically using the Landau-Zener method. The comparison shows that the wavepacket dynamics can be used for both the excitation and the quenching processes at energies ranging from 0.01 to 0.02 Hartree above the activation energy up to the energies of the order of 10 Hartree.

DOI: 10.1103/mgff-cjs8

I. INTRODUCTION

This study presents a comprehensive investigation of inelastic processes in collisions between atoms and/or atomic ions based on a two-dimensional nonadiabatic wavepacket dynamics approach. The validity of this treatment was initially noted in the Appendix of Ref. [1], where cross sections for charge transfer in collisions between hydrogen ions and nitrogen atoms were verified using a quantum scattering approach.

To our knowledge, the only previous attempt to apply two-dimensional dynamics to an inelastic atom-ion process was reported by Łabuda *et al.* [2]. However, that work did not include verification against quantum scattering calculations or other independent methods, and it was limited to relatively low collision energies.

We will here further investigate the validity of the two-dimensional wavepacket approach by studying both excitation and deexcitation (quenching) in the

$$N^+(^3P) + He(^1S) \leftrightarrow N^+(^1D) + He(^1S)$$

scattering processes. In case of quenching, the deexcitation energy is transferred to kinetic energy of the helium atom, so this process is superelastic scattering. To model the reaction, multistate scattering is needed where two pairs of spin-orbit coupled states are included. The potential energy curves and the effective spin-orbit couplings are here calculated *ab initio*. In the present study, the cross sections for excitation and deexcitation will be calculated using the two-dimensional wavepacket approach. The cross sections will then be compared with those calculated semiclassically (using a Landau-Zener model), and with cross sections obtained by solving the time-independent Schrödinger equation for the nuclear wave function using a logarithmic derivative method [3].

The presented approach is based directly on wavepacket dynamics on the coupled potential energy curves (PECs), which is a fundamentally different approach from close-coupling approaches in which nuclear radial wavefunctions are represented as wavepackets [4–6].

In chemical research, low-dimensional nonadiabatic wavepacket dynamics is often used to validate various surface hopping algorithms [7,8]. Furthermore, it often serves as a reference for developing novel semiclassical frameworks, such as those based on the Exact Factorization of the electron-nuclear wavefunction, ensuring that approximate algorithms correctly capture complex features such as quantum decoherence [9]. Wavepacket dynamics is also used for rate constants of simple chemical reactions. In this case, the overcoming of the energy barrier of the potential energy surface is usually investigated, but sometimes also nonadiabatic transitions are studied [10,11]. A recent application of nonadiabatic wavepacket dynamics that incorporates spin-orbit coupling is the study of nitrogen atom recombination in the photodissociation of N_2 [12], which utilizes a one-dimensional wavepacket dynamics approach.

*Contact author: marcin.buchowiecki@usz.edu.pl

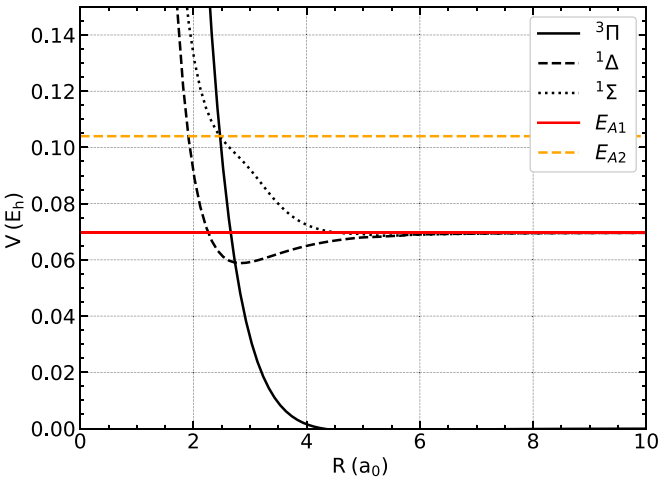

FIG. 1. The potential energy curves used for the cross-section calculations: $^3\Pi$ state with the $N^+(^3P)$–$He(^1S)$ dissociation limit and $^1\Delta$ and $^1\Sigma$ with the $N^+(^1D)$–$He(^1S)$ dissociation limit. Activation energies of both excitations (E_{A1} and E_{A2}) are shown.

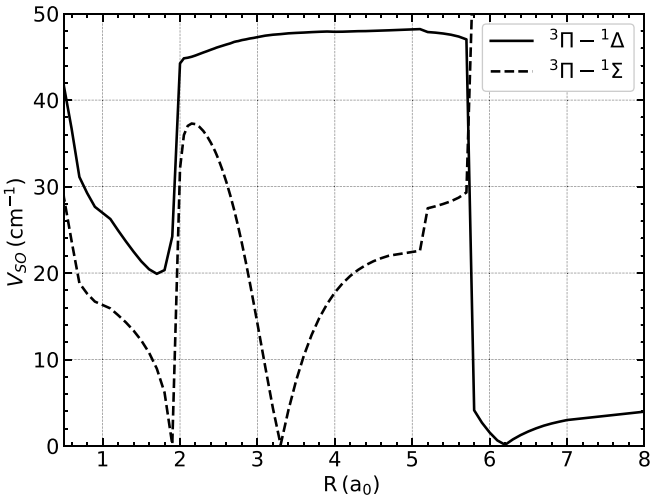

FIG. 2. The spin-orbit coupling constants for each pair of crossing states. The figure shows the calculated couplings before the asymptotic couplings are transformed away.

The N^+-He collisions are chosen because the excitation and quenching dynamics depends only on the spin-orbit couplings, and there are only two such couplings. This makes the system the simplest case for studying multistate scattering. In addition, these collisions could also be relevant for understanding various air/nitrogen and helium-containing plasmas [13], particularly nitrogen-seeded fusion plasmas [14,15], where helium and nitrogen atoms at different ionization states are produced and may interact [16]. The processes studied here may be additionally relevant for modeling conditions in the European Shock-Tube for High-Enthalpy Research (ESTHER), where helium is mixed with oxygen or nitrogen [17].

Previous work has focused on collisions of excited nitrogen ions with helium, which lead to charge transfer and do not proceed via spin-orbit coupling mechanisms [18]. Related processes, such as charge exchange in He^+ and He^{2+} collisions with neon, have been studied both experimentally and using the classical overbarrier model with empirical corrections [19]. However, the processes studied here are distinct from these previous works.

Throughout the article we use atomic units, unless otherwise specified.

II. METHODS

A. Potential energy curves and couplings

For the scattering process, relevant states are the spin-orbit coupled states $^3\Pi$, $^1\Sigma^+$, and $^1\Delta$ of the N^+-He system with potential energy curves crossing each other. These potential energy curves are calculated *ab initio* and are displayed in Fig. 1. The noncrossing potentials will have a negligible effect compared to the crossing ones. The potential energy curves are obtained using the MOLPRO package [20] with the MRCI-F12 method using the (6,3,3,2) active space of orbitals in C_{2v} symmetry. The cc-pVQZ-f12 basis set is used and the calculations are carried out in the large range of internuclear distances between 0.1 and 30 bohr.

The calculated potential energy curves obtained here were previously studied in [21] using CASSCF/MRCI (Complete Active Space Self-Consistent Field/Multi-Reference Configuration Interaction) with a smaller active space, but extrapolations of the potentials at both long and short distances were performed. The potential energy curves obtained in [21] are in good agreement with the ones calculated here.

All molecular states with potentials associated with the lower dissociation limit $[N^+(^3P) + He]$ have multiplicity 3; and all states associated with the higher dissociation limit $[N^+(^1D)+He]$ have multiplicity 1. Because of that, the spin-orbit coupling is the only coupling mechanism; there is no contribution from radial or rotational couplings among the states.

The effective spin-orbit coupling constants, V_{SO}, are obtained from the full spin-orbit matrix calculated using MOLPRO, for the singlet-triplet coupling, according to [22–24]

$$V_{SO} = \sqrt{\sum_{M,M'} \left|H^{SO}_{SM,S'M'}\right|^2}, \tag{1}$$

where the spin-orbit matrix elements are calculated with combination of the full Breit-Pauli operator and mean-field one-electron Fock operator. The coupling constants are also calculated at distances of 0.1–30 bohr. Studies of low-energy collisions explicitly treat fine atomic states and use individual elements of the spin-orbit matrix [25], rather than the effective ones. A recent example of using effective spin-orbit coupling in atom-molecule collisions is given in Ref. [26]. The effective spin-orbit coupling constants are shown in Fig. 2, where the sharp variations are also observed in other systems [27].

The potential matrix for the spin-orbit coupled states is given by

$$\mathbf{V}(R) = \begin{pmatrix} V_1(R) & V_{12}(R) & V_{13}(R) \\ V_{21}(R) & V_2(R) & 0 \\ V_{31}(R) & 0 & V_3(R) \end{pmatrix}, \tag{2}$$

where $V_1(R)$, $V_2(R)$, and $V_3(R)$ are the potentials of the $^3\Pi$, $^1\Delta$, and $^1\Sigma^+$ states, respectively. The effective spin-orbit

TABLE I. Parameters of the crossings: interatomic distance r_x, difference of derivatives $\mathrm{DF} = |dV_1/dR - dV_2/dR|$, and the coupling constant V_{SO} at the crossings. Atomic units are used.

$^3\Pi$ - $^1\Delta$	$^3\Pi$ - $^1\Sigma$
$r_{x1} = 2.7342$	$r_{x2} = 2.4687$
$\mathrm{DF}_1 = 0.12509$	$\mathrm{DF}_2 = 0.18857$
$V_{\mathrm{SO1}} = 2.132 \times 10^{-4}$	$V_{\mathrm{SO2}} = 1.538 \times 10^{-4}$

couplings between $^3\Pi$ and $^1\Delta$ are $V_{12}(R)$ and $^3\Pi$–$^1\Sigma^+$ is $V_{13}(R)$; for simplicity of notation, the SO subscript is omitted in the couplings. For the spin-orbit couplings $V_{ij}(R) = V_{ji}(R)$. Since the spin-orbit coupling elements are nonzero asymptotically at large distances (see Fig. 2), we make a constant similarity transformation of the diabatic potential matrix (2), such that the asymptotic coupling is transformed away:

$$\tilde{\mathbf{V}}(R) = \mathbf{T}_0^T \mathbf{V}(R) \mathbf{T}_0. \tag{3}$$

Here $\mathbf{T}_0$ is the constant orthogonal transformation matrix that transforms the states such that the diabatic potentials are uncoupled in the asymptotic region: $\tilde{V}_{ij}(R_\infty) = \tilde{V}_i(R_\infty)\delta_{ij}$, where $\tilde{V}_i(R_\infty)$ is the asymptotic energy of channel i when the spin-orbit coupling is considered.

In collisions between the ground state ions and atoms, $\mathrm{N}^+(^3\mathrm{P}) + \mathrm{He}(^1\mathrm{S})$, molecular ($\Lambda$-$S$) states of $^3\Pi$ and $^3\Sigma^-$ can be formed. In addition, molecular states of $^1\Delta$, $^1\Pi$, and $^1\Sigma^+$ symmetries are associated with the limit $\mathrm{N}^+(^1\mathrm{D})$+$\mathrm{He}(^1\mathrm{S})$. As discussed above, the effective spin-orbit coupling will couple the states of $^3\Pi$ symmetry to the $^1\Delta$ and $^1\Sigma^+$ states. When calculating the cross sections, the probability for forming one of the coupled states has to be considered. These probabilities are given by the ratio of the degeneracy factor for the specific molecular state to the sum of degeneracies from all molecular states formed by the reactants. In the case of $\mathrm{N}^+(^3\mathrm{P}) + \mathrm{He}(^1\mathrm{S})$ collisions, the probability is $g_1 = g(^3\Pi) = 2/3$, while for $\mathrm{N}^+(^1\mathrm{D})$+$\mathrm{He}(^1\mathrm{S})$, the factors are $g_2 = g(^1\Delta) = 2/5$ and $g_3 = g(^1\Sigma^+) = 1/5$.

B. Landau-Zener method

The excitation and quenching cross sections can be calculated semiclassically using a multistate Landau-Zener model. In the Landau-Zener model, the survival probability (probability to remain in the same crossing potential) is given by

$$p(E, b) = \exp\left(-\pi \sqrt{\frac{2\mu}{E - b^2 E/R_x^2 - E_A}} \frac{V_{\mathrm{SO}}^2}{dF}\right). \tag{4}$$

Here, the impact parameter is b and the energy of the collision is E. The internuclear distance of the crossing of the two potentials is R_x, μ is the reduced mass of the system, E_A is the activation energy of the process (i.e., the minimum energy for the process to occur), and $dF = |dV_1/dR - dV_2/dR|$ are derivatives of the potential energy curves, taken at the crossing point. The probability is zero when the factor under the square root is less than or equal to zero. The probability of transition to the other PECs at the crossing is then $1 - p(E, b)$. The parameters of both crossings, needed for calculation of probabilities below, are given in Table I, where all values are given in atomic units.

For the excitation process $\mathrm{N}^+(^3\mathrm{P})$–$\mathrm{He}(^1\mathrm{S}) \rightarrow \mathrm{N}^+(^1\mathrm{D})$–$\mathrm{He}(^1\mathrm{S})$, the reaction is activated at energy $E_{A1} = 0.069\,67$ Hartree and occurs with a single crossing. When the energy of collision reaches $E_{A2} = 0.1040$ Hartree, the higher crossing becomes available, and the appropriate probability has to be calculated considering all possible paths (multistate Landau-Zener theory). The resulting excitation probability is the following (assuming the process is active, i.e., $E > E_{A1}$):

$$P_{\mathrm{excit}} = \begin{cases} g_1 2p_1(1-p_1) & \text{for } E < E_{A2} \\ g_1 2p_1 p_2(1-p_2) + g_1 p_1(1-p_1)[1 + p_2^2 + (1-p_2)^2] & \text{for } E \geqslant E_{A2}, \end{cases} \tag{5}$$

where p_1 is the survival probability at the $^3\Pi$ - $^1\Delta$ (lower energy) crossing and p_2 is the survival probability at the $^3\Pi$ - $^1\Sigma$ (higher energy) crossing. The factors g_i are the statistical factors discussed in Sec. II A. Activation energy (i.e., the energy at which the probability is nonzero) is E_{A1} for p_1 and E_{A2} for p_2. The second of the expressions in (5) agrees with the probabilities given in [28], which considers a different quenching-type process.

The quenching process $\mathrm{N}^+(^1\mathrm{D})$–$\mathrm{He}(^1\mathrm{S}) \rightarrow \mathrm{N}^+(^3\mathrm{P})$–$\mathrm{He}(^1\mathrm{S})$ is active at all nonzero collision energies. At energies below E_{A2}, only the probability p_1 is nonzero [the activation energy in Eq. (4) is zero] and when the collision energy reaches E_{A2} the probability p_2 activates [with the activation energy $E_{A2} - E_{A1}$ in Eq. ((4). The corresponding probability of quenching becomes

$$P_{\mathrm{quench}} = \begin{cases} g_2 2p_1(1-p_1) & \text{for } E < E_{A2} - E_{A1} \\ g_3 2p_1 p_2(1-p_2) + g_2 p_1(1-p_1)[1 + p_2^2 + (1-p_2)^2] & \text{for } E \geqslant E_{A2} - E_{A1}. \end{cases} \tag{6}$$

The cross sections of excitation and quenching are calculated from the nonadiabatic process probability:

$$\sigma(E) = 2\pi \int_0^\infty bP(E, b)db. \tag{7}$$

Note that there is no restriction on the integration limit, because the probabilities are defined to be zero if the expression under the square root in Eq. (4) is less than or equal to zero.

The cross sections can also be calculated with the sum of the transition probabilities generated by both crossing points treated separately. It turns out that the difference between the multistate cross section and the sum of single-crossing cross sections is of the order of 10^{-4}–10^{-5} a.u. The

difference in probabilities in both cases is $2p_2(1-p_2)(1-p_1)$
$(g_b - g_a p_1)$, where g_a and g_b are connected to appropriate reaction channels. That expression is always small in the case of weak coupling (p approaching 1 results in $1-p$ approaching zero).

This result suggests that the quantum scattering and wavepacket dynamics approaches can be treated as a simple sum of two separate processes.

C. Quantum scattering

The cross sections can be computed by solving the time-independent coupled Schrödinger equation for the nuclear wave function. Using a partial wave expansion of the nuclear wave functions for the coupled states, the radial wave functions satisfy a time-independent coupled Schrödinger equation

$$\left[2\mu\frac{d^2}{dR^2} + \frac{\ell(\ell+1)}{2\mu R^2}\right]u_{i,\ell}(R) = \sum_{j=1}^{3}\tilde{V}_{ij}(R)u_{j,\ell}(R) = Eu_{i,\ell}(R), \tag{8}$$

with the boundary condition $u_{i,\ell}(R_0) = 0$. With appropriate boundary conditions for $u'_{i,\ell}(R_0)$, three linearly independent solutions can be formed that are combined into the 3×3 matrix $\mathbf{u}_\ell(R)$.

By introducing the logarithmic derivative of the radial wave function, $\mathbf{y}_\ell(R) = \mathbf{u}'_\ell\mathbf{u}_\ell^{-1}$, the coupled Schrödinger equation (8) can be transformed into a matrix Riccati equation [3,29]

$$\mathbf{y}'_\ell + \mathbf{Q}_\ell + \mathbf{y}_\ell^2 = \mathbf{0}, \tag{9}$$

where $\mathbf{Q}_\ell = 2\mu[E\mathbf{1} - \tilde{\mathbf{V}}(R)] - \frac{\ell(\ell+1)}{R^2}\mathbf{1}$.

Johnson [3,29] developed an efficient algorithm to numerically solve the matrix Riccati equation. This has been used from $R_0 = 0.5a_0$ to $R_{\text{stop}} = 30a_0$ in the steps of $dR = 0.005a_0$. From the asymptotic value of the logarithmic derivative, the scattering matrix $\mathbf{S}_\ell$ can be calculated (see [3] for expressions). The cross section for inelastic scattering $j \to i$ is then given by

$$\sigma_{ij}(E) = g_j\frac{\pi}{k_j^2}\sum_{\ell=0}^{\ell_{\max}}(2\ell+1)|S_{ij}^\ell - \delta_{ij}|^2. \tag{10}$$

Here, the asymptotic wave number is $k_j = \sqrt{2\mu(E - V_j^{\text{th}})}$ with V_j^{th} being the corresponding threshold energy. g_j is the statistical factor discussed in Sec. II A. The summation in Eq. (10) is terminated when the ratios of the partial cross sections to the accumulated integral cross sections remained less than 3×10^{-5} for 100 terms in succession.

D. Two-dimensional nonadiabatic wavepacket dynamics

The nonadiabatic wavepacket dynamics are simulated using the split-operator method. This approach, also known as Strang splitting, is a general numerical technique for solving partial differential equations, which, in the present context, is the time-dependent Schrödinger equation. The formal solution can be written as

$$|\Psi(t)\rangle = \mathrm{e}^{-\mathrm{i}t\mathbf{H}}|\Psi(0)\rangle, \tag{11}$$

where $|\Psi(0)\rangle$ is the initial wavefunction and $\mathbf{H} = \mathbf{T} + \mathbf{V}$ is the Hamiltonian. Because the kinetic energy operator $\mathbf{T}$ and potential energy operator $\mathbf{V}$ do not commute, the time evolution operator for a small time step Δt is approximated using a second-order splitting as

$$\mathrm{e}^{-\mathrm{i}\Delta t\mathbf{H}} \approx \mathrm{e}^{-\mathrm{i}(\Delta t/2)\mathbf{V}}\mathrm{e}^{-\mathrm{i}\Delta t\mathbf{T}}\mathrm{e}^{-\mathrm{i}(\Delta t/2)\mathbf{V}}. \tag{12}$$

This factorization allows the kinetic and potential propagators to be applied sequentially. Furthermore, because the kinetic operator is diagonal, it is evaluated efficiently using Fourier transforms. The final expression for propagating the wavefunction over a single time step Δt is

$$\langle\mathbf{R}|\Psi(t+\Delta t)\rangle = \mathrm{e}^{-\mathrm{i}(\Delta t/2)\mathbf{V}}\mathcal{F}^{-1}[\mathrm{e}^{-\mathrm{i}\Delta t\mathbf{T}}\mathcal{F}\{\mathrm{e}^{-\mathrm{i}(\Delta t/2)\mathbf{V}}\langle\mathbf{R}\,|\,\Psi(t)\rangle\}], \tag{13}$$

where $\langle\mathbf{R}|\Psi(t+\Delta t)\rangle$ denotes the wavefunction in position representation. By iteratively applying this procedure to an initial wavefunction, the system can be propagated arbitrarily forward in time. In the present work, this split-operator propagation scheme was employed as implemented in the ZINQ software package [30].

In this study, we employ the Split-Operator method to propagate a wavepacket on a two-dimensional Cartesian grid. The system is defined by two independent Cartesian degrees of freedom: a longitudinal axis, $\mathbf{z}$ (which spans both negative and positive values along the collision path), and a transverse axis, b (corresponding to the impact parameter and can be chosen to be either on the x or the y axis); internuclear distance is then $R = \sqrt{z^2 + b^2}$. By treating these coordinates as independent Cartesian variables, the specific Hamiltonian used can be written in the diabatic basis as

$$\mathbf{H} = \mathbf{T} + \mathbf{V} = -\frac{1}{2m}\left(\frac{\partial^2}{\partial\mathbf{z}^2} + \frac{\partial^2}{\partial b^2}\right)\otimes\mathbf{I}_N + \mathbf{V}(R), \tag{14}$$

where I_N is the $N\times N$ identity matrix with N being the number of electronic states (we perform simulations for $N=2$ as well as $N=3$) and $\mathbf{V}(R)$ is the potential energy matrix defined by the curves in Fig. 1. The initial state of the system was defined as a two-dimensional Gaussian wavepacket of the form

$$\Psi(\mathbf{z}, b, 0) = \Omega\ \exp(-(\mathbf{z}-\mathbf{z_0})^2 - (b-b_0)^2 + \mathrm{i}p_0(\mathbf{z}-\mathbf{z_0})), \tag{15}$$

where Ω is the normalization constant, $(\mathbf{z_0}, b_0)$ denotes the initial coordinates of the center of the wavepacket, and p_0 is the initial momentum along the $\mathbf{z}$ coordinate corresponding to the desired collision energy, calculated as $p_0 = \sqrt{\frac{2m}{E}}$. No initial momentum in the b direction is applied. The standard deviation of the wavepacket can be extracted from Eq. (15) and is equal to $\sigma^2 = \frac{1}{2}$ in both directions. For all simulations, the initial separation was set to $\mathbf{z_0} = 10$ bohr. The coordinate grid chosen for all simulations is $\mathbf{z}\in[-12, 16]$ bohr and $b\in[-12+b_0, 12+b_0]$ bohr. These dimensions are specifically chosen to ensure that the wavepacket remains fully contained

within the simulation region, thereby minimizing nonphysical interactions or reflections at the grid boundaries.

To evaluate the excitation and quenching cross sections, a large set of wavepacket simulations are performed over a grid of impact parameters b and initial kinetic energies E. This approach systematically samples the two-dimensional probability function $P(E, b)$ required for the cross-section calculations, with each point on the $P(E, b)$ surface corresponding to an independent dynamical simulation. While an alternative approach exists using an extremely broad wavepacket in conjunction with analysis of the asymptotic flux [31,32], we deliberately chose this sampling strategy. Propagating an extremely wide wavepacket requires a large spatial grid and careful placement of complex absorbing potentials (CAPs), which can be memory prohibitive and is prone to boundary artifacts. Our approach uses fairly localized wavepackets on a relatively small grid, ensuring minimal interaction with grid edges. Additionally, since the simulations are independent, they can be massively parallelized.

The state-specific transition probability was obtained directly from the final population of the target state i, calculated as $\langle\Psi_i(t_{\text{final}})|\Psi_i(t_{\text{final}})\rangle$. Here, t_{final} represents an asymptotic time at which the wavepacket has left the interaction region and the probability flux between the electronic states has completely ceased. For the simulations in this work, t_{final} ranges from approximately 20 000 a.u. for the slowest simulations ($E = 0.001$ a.u.) to 300 a.u. for the fastest simulations ($E = 10$ a.u.).

The calculations are divided into three energy regimes to optimize computational resources. For energies between 0.0 and 0.5 Hartree, a grid of 512 points is used. For energies between 0.5e and 1.0 Hartree, a grid of 1024 points is employed, and for energies between 1.0 and 10.0 Hartree, a grid of 2048 points is utilized. The time step for all simulations is set to 1 a.u. To ensure the accuracy of the results, all simulations are verified for convergence with respect to both the grid size and the time step.

Probabilities $P(E, b)$ are calculated at 25 values of the impact parameter b that ranged from zero to 10 bohr at each energy. The calculated probabilities are interpolated using the two-dimensional RectBivariateSpline python procedure, and the resulting function is used in the integration to compute the cross section according to Eq. (7), including appropriate statistical factors.

III. RESULTS

The wavepacket dynamics is performed for excitation and quenching including two crossings, $^3\Pi$ - $^1\Delta$ and $^3\Pi$ - $^1\Sigma$, with both two-state and multistate approaches.

The wavepacket dynamics is significantly more time-consuming than the time-independent quantum scattering calculations. Therefore, according to the analysis of the Landau-Zener results in Sec. II B, the wavepacket cross sections for the overall process can be approximated as the sum of cross sections of both crossing pairs of potentials. The calculated cross sections are presented in Figs. 3–10, where both quantum scattering and wavepacket cross sections are calculated with the full multistate approach. The excitation is also tested for applicability of the two-state approximation.

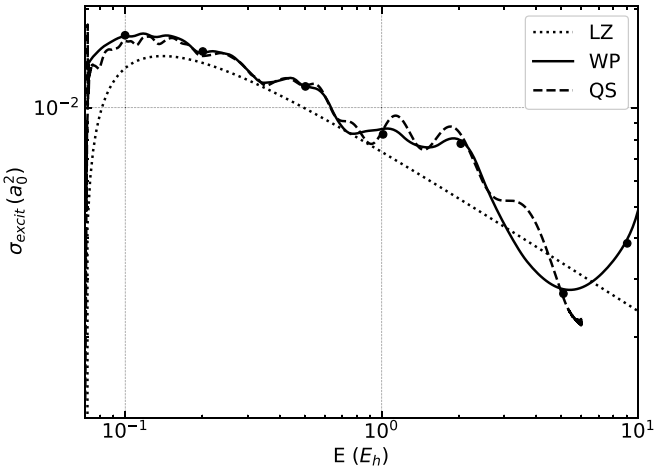

FIG. 3. Excitation cross section for the $^3\Pi \rightarrow {}^1\Delta$ transition from Landau-Zener (LZ), wavepacket (WP), and quantum scattering (QS) methods. Results from the two-state wavepacket approach are also shown as black dots.

The quantum excitation cross sections for the $^3\Pi \rightarrow {}^1\Delta$ transition agree very well in the 0.08–0.7 Hartree region (Fig. 3). At the lowest energies, just above the barrier, the wavepacket result fails to reproduce the fast increase of the cross section (Fig. 4). At collision energies over 1 Hartree, a discrepancy between quantum scattering and wavepacket dynamics is present. In the quantum scattering approach, analytical asymptotic functions are combined with the value of the logarithmic derivative at the boundary to compute the scattering matrix [3]. For scattering energies above 6 Hartree, the routine for computing these functions (Riccati-Bessel functions of the first and second kind) have numerical challenges and an energy of 10 Hartree could not be reached. The two-state wavepacket approach correctly reproduces the multistate result.

The coupling between the $^3\Pi$ and $^1\Delta$ states is very weak at large distances, and wavepacket dynamics yielded the

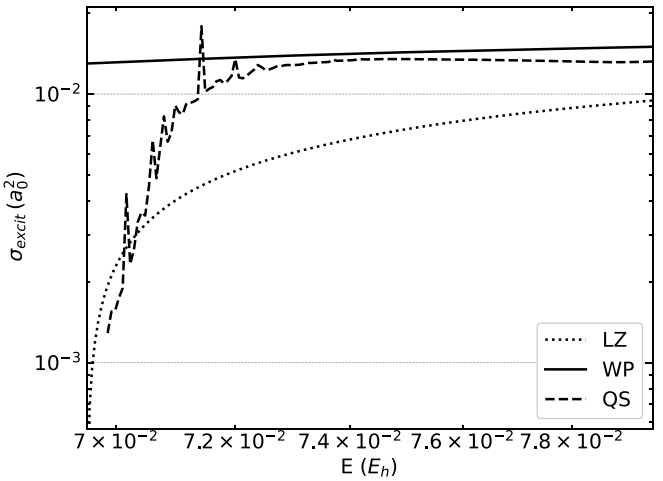

FIG. 4. Low-energy excitation cross section for the $^3\Pi \rightarrow {}^1\Delta$ transition from Landau-Zener (LZ), wavepacket (WP), and quantum scattering (QS) methods.

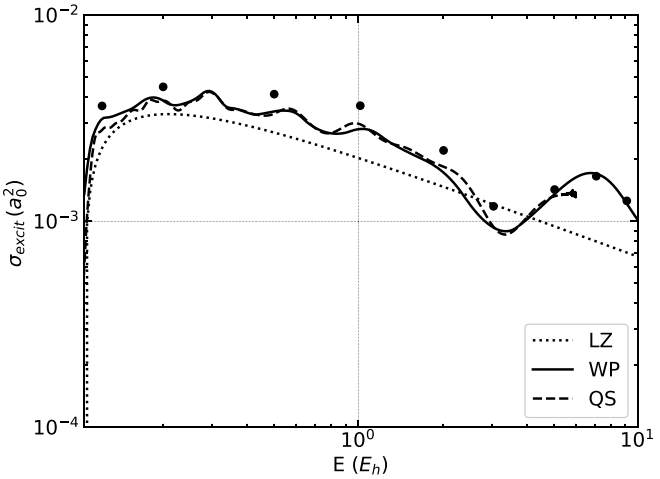

FIG. 5. Excitation cross sections for the $^3\Pi \rightarrow {}^1\Sigma$ transition from Landau-Zener (LZ), wavepacket (WP), and quantum scattering (QS) methods. Results from the two-state wavepacket approach are also shown as black dots.

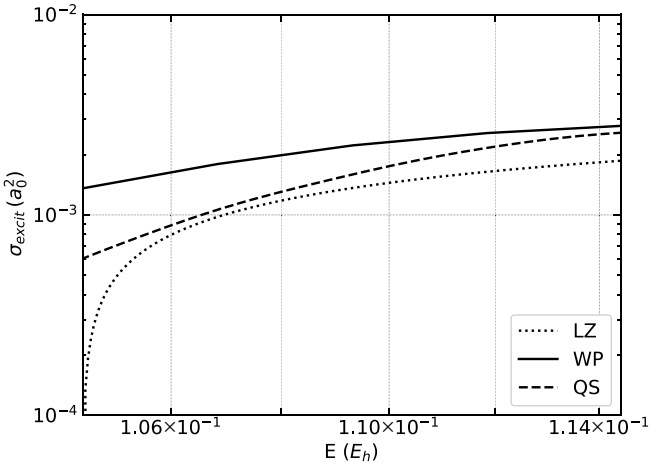

FIG. 6. Low-energy excitation cross section for the $^3\Pi \rightarrow {}^1\Sigma$ transition from Landau-Zener (LZ), wavepacket (WP), and quantum scattering (QS) methods.

same results with both transformed and untransformed potentials and couplings. The conclusion is that the theoretical description of the scattering process does not always require a transformation to obtain exact zero couplings at large distances, but sometimes oscillations are negligibly small compared with the probability.

Figure 5 presents the cross section for the $^3\Pi \rightarrow {}^1\Sigma$ transition. This cross section is smaller because of the higher activation energy. The agreement between the wavepacket and quantum scattering is very good, but the two-state approach does not recover a multistate result (but in absolute values, the discrepancy is small). In this case, the wavepacket dynamics is performed on transformed potentials and couplings because the much higher coupling at large distances caused strong oscillations (not only at the end of the dynamics but from the beginning of the simulations) and resulted in completely incorrect results.

At low energies (see Fig. 6), the discrepancy of wavepacket and quantum scattering results increases below 0.01 Hartree above the activation energy. The calculated total excitation cross sections are displayed in Fig. 7, and above 1 Hartree, the discrepancies are slightly reduced compared with Fig. 3.

The results for the quenching process are shown in Figs. 8–10. Again, the agreement of the wavepacket and quantum scattering methods is very good, from around 0.01 Hartree above the activation energy (which is zero for the quenching) up to energies above 1 Hartree. In general, the agreement is even better than for the excitation process.

Finally, some general conclusions can be drawn regarding all cases. The highly changeable character of the couplings leads to less regular behavior of the cross sections than in the previously studied case [1]. In the present case, the cross sections also have some broad oscillations, but not around the Landau-Zener values as in Ref. [1]. Nonadiabatic radial (derivative) couplings usually have a more or less pronounced maximum and approach zero at long and short distances [33]. It can be concluded that spin-orbit induced processes exhibit

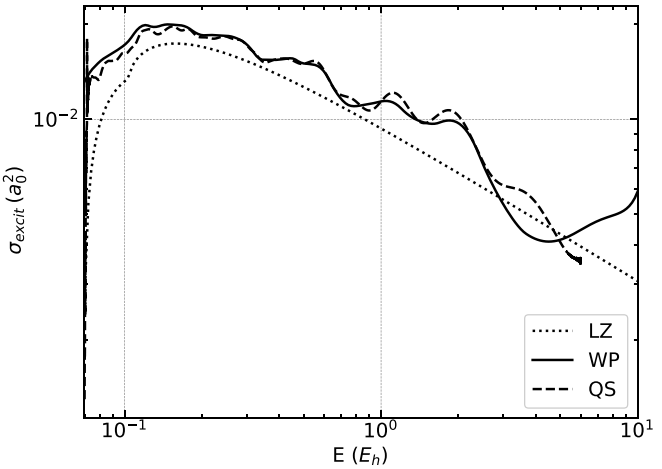

FIG. 7. The total cross section for the $N^+(^3P) + He(^1S) \rightarrow N^+(^1D)$–$He(^1S)$ excitation process.

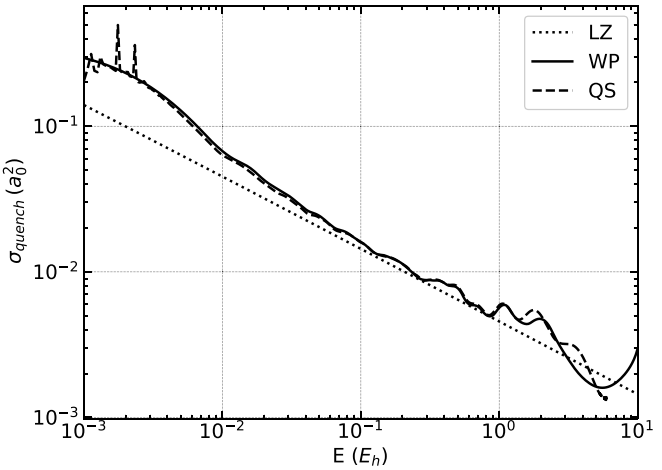

FIG. 8. Quenching cross section for the $^1\Delta \rightarrow {}^3\Pi$ transition from Landau-Zener (LZ), wavepacket (WP), and quantum scattering (QS) methods.

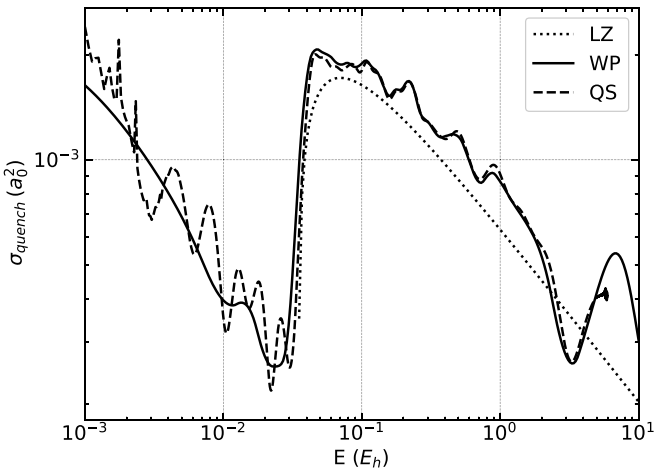

FIG. 9. Quenching cross section for the $^1\Sigma \rightarrow {}^3\Pi$ transition from Landau-Zener (LZ), wavepacket (WP), and quantum scattering (QS) methods.

more complex dynamics because their couplings have a more intricate structure.

Previous studies show that the Landau-Zener method underestimates cross sections and rate constants at low energies above the barrier [1,34]. The same is observed in this study for most energies.

Inspection of all the cases studied here, and also nitrogen-proton collisions in Ref. [1], allows us to conclude that two-dimensional wavepacket dynamics can be used above around 0.01 Hartree over the activation energy of a given process, and agreement with quantum scattering results is very good.

In this study, the two-dimensional wavepacket dynamics is applicable up to energies of 10 Hartree (Ref. [1]), where the quantum scattering approach may be more prone to numerical errors than wavepacket dynamics. Above the thresholds, the cross sections computed using the time-independent quantum scattering approach exhibit resonances not observed in the wavepacket results. These resonances are challenging to capture with the wavepacket method. In general, the Landau-Zener method can be used as a qualitative estimation of the cross sections.

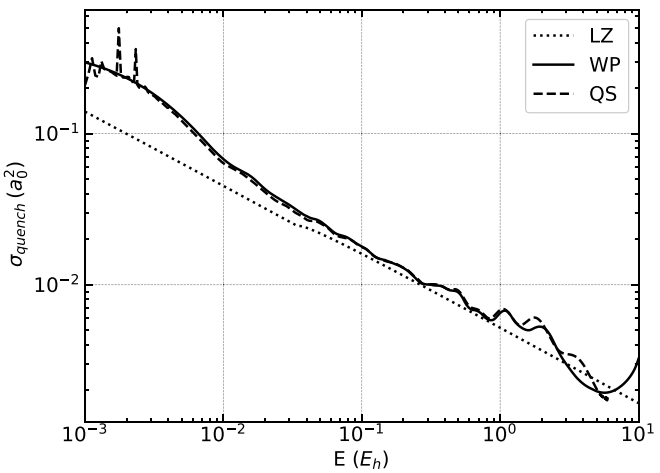

FIG. 10. The total cross section for the $N^+(^1D)$+$He(^1S)$→ $N^+(^3P)$–$He(^1S)$ quenching process.

At high energies, more channels are open and may limit accuracy of the results but also at higher energies interference effects are in general lower and the other channels become less and less coupled with an increase of the energetic distance of higher channels.

The cross sections for the excitation and quenching processes are provided as Supplemental data in the energy range (E_{x1},10), calculated using both the wavepacket and the quantum scattering methods.

IV. CONCLUSIONS

The two-dimensional nonadiabatic wavepacket dynamics is shown to be useful in treating the spin-orbit induced inelastic transitions in atomic collisions. The energy range of applicability spans from around 0.01 Hartree above the activation energy to 10 Hartree and higher, where the quantum scattering method may be prone to numerical errors. This allows for the treatment of collisions of atoms and atomic ions at energies of the order of 1 keV.

The advantage of the wavepacket approach at high energies comes at the expense of a significantly higher computational cost. The disadvantage of the presented wavepacket approach is the inability to recover the resonant structure at the lowest energies above the activation barrier. For a proper description of a low-energy behavior of cross sections, a very wide wavepacket, according to the uncertainty principle, is needed but it would significantly increase the computational cost.

The proposed wavepacket approach seems to be the simplest in terms of theory—it is based on the Fourier transform, whereas scattering theory, based on plane waves, is more involved. Because of that, the wavepacket approach should have potential for use by nonexperts.

ACKNOWLEDGMENTS

T.J. thanks the Czech Science Foundation for support via Grant No. 24-11466S. Å.L. acknowledges support by the Knut and Alice Wallenberg Foundation through the project "Making and Breaking of Molecular Bonds" under Contract No. 2024.0134.

DATA AVAILABILITY

Supplemental data are attached and described in the Appendix. The raw data from calculations made by T.J. have been stored on Zenodo [35].

APPENDIX

The potential energy curves and spin-orbit couplings used in this study are given in the files NpHe_PECs.txt and Vso.txt, respectively. All described files are available at [36]. The cross sections for the excitation process are given in sigma_ex_WP.txt and sigma_ex_QS.txt for the wavepacket and quantum scattering, respectively; similarly, the data for quenching are given in sigma_quench_WP.txt and sigma_quench_QS.txt.

[1] M. Buchowiecki and T. Jíra, Spin–orbit induced charge transfer in $H^+/D^+/T^+$-N(^4S) collisions, J. Quant. Spectrosc. Radiat. Transfer **347**, 109697 (2025).

[2] M. Łabuda, J. González-Vázquez, F. Martín, and L. González, A non-adiabatic wavepacket dynamical study of the low energy charge transfer process in the $S^{3+} + H$ collision, Chem. Phys. **400**, 165 (2012).

[3] B. R. Johnson, The multichannel log-derivative method for scattering calculations, J. Comput. Phys. **13**, 445 (1973).

[4] E. Baloïtcha, M. Desouter-Lecomte, M.-C. Bacchus-Montabonel, and N. Vaeck, Wave packet methods for charge exchange processes in ion-atom collisions, J. Chem. Phys. **114**, 8741 (2001).

[5] N. Vaeck, M.-C. Bacchus-Montabonel, E. Baloïtcha, and M. Desouter-Lecomte, Time-dependent wave-packet treatment of the $Si^{4+} + He$ collision, Phys. Rev. A **63**, 042704 (2001).

[6] M. Y. Yakovlev and A. K. Belyaev, Wave-packet study of the mutual neutralization processes in low-energy lithium-hydrogen collisions, Phys. Rev. A **112**, 052827 (2025).

[7] A. Jain and A. Sindhu, Pedagogical overview of the fewest switches surface hopping method, ACS Omega **7**, 45810 (2022).

[8] T. Jíra, J. Janoš, and P. Slavíček, Critical assessment of curvature-driven surface hopping algorithms, J. Chem. Theory Comput. **21**, 9784 (2025).

[9] B. F. E. Curchod, F. Agostini, and E. K. U. Gross, An exact factorization perspective on quantum interferences in nonadiabatic dynamics, J. Chem. Phys. **145**, 034103 (2016).

[10] J. Zhao, A quantum time-dependent wave-packet study of intersystem crossing effects in the $O(^3P_{0,1,2}) + D_2(v = 0, j = 0)$ reaction, J. Chem. Phys. **138**, 134309 (2013).

[11] Y. Mao, Z. Yang, B. Buren, and M. Chen, Unveiling quantum interference in the $D^+ + H_2$ nonadiabatic reaction dynamics at low collision energies, J. Phys. Chem. A **128**, 420 (2024).

[12] N. Gelfand, F. Remacle, and R. D. Levine, Recombination of N atoms in a manifold of electronic states simulated by time-reversed nonadiabatic photodissociation dynamics of N_2, J. Phys. Chem. Lett. **14**, 4625 (2023).

[13] S. D. Dongarwar, T. Zhu, M. Baeva, R. Brandenburg, A. Bhan, F. Sigeneger, and P. J. Bruggeman, Nitric oxide decomposition in a helium radio frequency atmospheric pressure plasma: Kinetic and transport processes, J. Phys. D: Appl. Phys. **58**, 495202 (2025).

[14] L. Casali, D. Eldon, A. McLean, T. Osborne, A. Leonard, B. Grierson, and J. Ren, Impurity leakage and radiative cooling in the first nitrogen and neon seeding study in the closed DIII-D SAS configuration, Nucl. Fusion **62**, 026021 (2022).

[15] I. Senichenkov, A. Poletaeva, E. Kaveeva, I. Veselova, A. Nichik, and V. Rozhansky, Comparison of divertor seed impurity gases retention efficiency by SOLPS-ITER modeling, Nucl. Fusion **65**, 056042 (2025).

[16] A. Zito, O. Pan, M. Wischmeier, A. Kappatou, A. Kallenbach, S. Makarov, M. Bernert, M. Cavedon, D. Reiter, U. Stroth, and the ASDEX Upgrade Team, SOLPS-ITER modelling of helium transport, recycling and pumping at the ASDEX upgrade tokamak, Nucl. Fusion **65**, 046022 (2025).

[17] M. L. da Silva, R. Ferreira, J. Vargas, R. Rodrigues, B. Carvalho, L. Alves, B. Gonçalves, A. Smith, J. Merrifield, S. McDowell, *et al.*, European shock-tube for high enthalpy research: Design and instrumentation, manufacturing, and acceptance testing, in *AIAA Scitech Forum, 2020* (American Institute of Aeronautics and Astronautics Inc., Reston, VA, 2020), pp. 1–11.

[18] M. Kimura, J. P. Gu, G. Hirsch, and R. J. Buenker, Electron capture in collisions of $N^+(^5S, ^3P)$ with He: The effect of metastable ions, Phys. Rev. A **51**, 2063 (1995).

[19] X. Hui, B. Ding, D. Yu, T. Guo, X. Song, T. Zhang, L. Kang, J. Li, X. Zhu, and X. Chen, Charge-exchange dynamics in He^+ and He^{2+} collisions with Ne and Ar at 0.63–1.41-a.u. velocities, Phys. Rev. A **112**, 012805 (2025).

[20] H.-J. Werner, P. J. Knowles, F. R. Manby, J. A. Black, K. Doll, A. Heßelmann, D. Kats, A. Köhn, T. Korona, D. A. Kreplin, Q. Ma, T. F. I. Miller, A. Mitrushchenkov, K. A. Peterson, I. Polyak, G. Rauhut, and M. Sibaev, The MOLPRO quantum chemistry package, J. Chem. Phys. **152**, 144107 (2020).

[21] S. Lias, L. Aissaoui, M. Bouledroua, and K. Alioua, Quantum-mechanical transport properties of $N + (^3P)$ and $N + (^1D)$ ions in a neutral gas made of helium, Mol. Phys. **118**, e1657601 (2020).

[22] G. Granucci, M. Persico, and G. Spighi, Surface hopping trajectory simulations with spin-orbit and dynamical couplings, J. Chem. Phys. **137**, 22A501 (2012).

[23] A. O. Lykhin, D. S. Kaliakin, G. E. dePolo, A. A. Kuzubov, and S. A. Varganov, Nonadiabatic transition state theory: Application to intersystem crossings in the active sites of metal-sulfur proteins, Int. J. Quantum Chem. **116**, 750 (2016).

[24] M. Rooein and S. A. Varganov, How to calculate the rate constants for nonradiative transitions between the m_s components of spin multiplets? Mol. Phys. **121**, e2116364 (2023).

[25] P. J. Dagdigian, M. H. Alexander, and J. Kłos, Theoretical investigation of the dynamics of $O(^1D \rightarrow ^3P)$ electronic quenching by collision with xe, J. Chem. Phys. **143**, 054306 (2015).

[26] B. R. L. Galvão, M. O. Alves, D. Lu, and H. Guo, Electronic quenching of $N(^2D)$ in collision with $CO(^1\Sigma^+)$ via spin-forbidden transitions, J. Chem. Phys. **162**, 154301 (2025).

[27] R. P. Brady, S. N. Yurchenko, G.-S. Kim, W. Somogyi, and J. Tennyson, An *ab initio* study of the rovibronic spectrum of sulphur monoxide (SO): Diabatic vs adiabatic representation, Phys. Chem. Chem. Phys. **24**, 24076 (2022).

[28] R. K. Janev, D. S. Belić, and B. H. Bransden, Total and partial cross sections for electron capture in collisions of hydrogen atoms with fully stripped ions, Phys. Rev. A **28**, 1293 (1983).

[29] D. E. Manolopoulos, M. J. Jamieson, and A. D. Pradhan, Johnson's log derivative algorithm rederived, J. Comput. Phys. **105**, 169 (1993).

[30] T. Jíra, tjira/zinq: v0.5.6 (Version v0.5.6) [Computer software], Zenodo, 2026, doi: 10.5281/zenodo.18387995.

[31] N. Vaeck, M. Desouter-Lecomte, and J. Liévin, Non-adiabatic wavepacket dynamics for charge-exchange processes in ion-atom collisions: Application to $C^{4+} + H$, J. Phys. B: At. Mol. Opt. Phys. **32**, 409 (1999).

[32] J. Loreau, S. Ryabchenko, and N. Vaeck, Charge transfer in proton–helium collisions from low to high energy, J. Phys. B: At. Mol. Opt. Phys. **47**, 135204 (2014).

[33] R. P. Brady, C. Drury, S. N. Yurchenko, and J. Tennyson, Numerical equivalence of diabatic and adiabatic representations in diatomic molecules, J. Chem. Theory Comput. **20**, 2127 (2024).

[34] M. Buchowiecki, Y. Wu, and G. C. Schatz, Elastic cross sections, excitation exchange cross sections, and rate constants for excitation and quenching in N(^4S)-N(^2D) collisions, At. Data Nucl. Data Tables **164**, 101728 (2025).

[35] T. Jíra, K. Bouzek, and Š. Paušová, Dataset for wavepacket dynamics and quantum scattering in spin-orbit induced excitation and quenching in N + (^{3}P)-He(^{1}S) and N +^{1} D)-He(^{1}S) collisions (Version 1) [Dataset] Zenodo, 2026, doi: 10.5281/zenodo.19390816.

[36] See Supplemental Material at http://link.aps.org/supplemental/10.1103/mgff-cjs8 for potential energies, couplings and cross sections.